AIAA SciTech Forum
12-16 January 2026, Orlando, FL
AIAA SCITECH 2026 Forum

10.2514/6.2026-1444

Feature-based Modeling for Aeroelastic Load Alleviation using Smart Vortex Generators

Adrian Beňo*, Jurij Sodja† and Xuerui Wang ‡
Delft University of Technology, Kluyverweg 1, 2629HS Delft, The Netherlands

We use feature-based modeling framework for control of loads on aeroelastic wings in the presence of unsteady wind gust disturbances, leveraging interpretable reduced-order-model system identification techniques without relying on black-box machine learning techniques. Unlike prior formulations, we explicitly include the dominant disturbance, such as a gust, as a control input within the model, allowing the controller to respond adaptively and in anticipation to external forcing. To this end, model predictive control (MPC) could be used in the low dimensional latent space of features, whose dynamics are identified partly by sparse identification of nonlinear dynamics with control (SINDYc) and linear parameter-varying system (LPV). As a proof of concept, the methodology is applied to system identification of smart vortex generators (SVGs) for mitigating transient gust loads on an aeroelastic wing section in CFD simulations. This methodology offers a promising path toward real-time mitigation of atmospheric disturbances in next-generation flight systems.

I. Introduction

Modern aircraft design tends toward high aspect ratio (AR) wings due to their significant benefits in terms of improved aerodynamic efficiency [1]. At the same time, the wing weight penalty needs to be minimized in order to capitalize on the potential fuel savings. Key technologies to help reach this objective are novel flight control systems for advanced active and passive loads alleviation. Gust load alleviation (GLA) is essential not only to prevent structural fatigue due to repetitive loading and potentially catastrophic single-event damage, but also to improve passenger comfort. Moreover, the significance of gust load mitigation extends beyond commercial aviation and is also crucial in other engineering applications, such as wind turbines and unmanned aerial vehicles. In this work, we explore novel flow control technique—smart vortex generators (SVGs)—shown in Figure 1, which offer a promising alternative [1]. Their working principle is to rotate perpendicular to the incoming flow in case of gust encounter in order to cause flow separation, resulting in locally decreased lift. Unlike their traditional counterparts (ailerons, flaperons [2, 3] and blown jets [4, 5]), SVGs allow low-latency actuation due to their small size*, which also makes them more economical in terms of the actuation energy expenditure. Moreover, SVGs can remain flush with the freestream direction during undisturbed flight, incurring minimal drag penalty.

Previous studies on SVGs [6–8] demonstrate that they can drastically reduce lift and wing root bending moment during gust encounter. However, current practice in SVG control exhibits significant limitations. Reference [7] demonstrated that a simple on–off control scheme for SVGs induces wing oscillations, especially after the gust has dissipated. These oscillations contradict the objective of reducing structural fatigue. To overcome these limitations, we propose active control for SVGs based on data-driven reduced-order model (ROM). Conventional approaches typically rely on full-state data-driven system identification combined with control strategies. However, flow complexity associated with gust-wing-SVG interactions can hardly be captured by ever more complex polynomial models, which is why deep neural networks (DNNs) have become so popular surrogates for dynamical models. Whereas DNNs can approximate complex dynamics, they often lack interpretability and are prone to overfitting or instability in control applications. We address this by primarily integrating explainable feature-based manifold modeling (FeMM) [9, 10], sparse identification of nonlinear dynamics with control (SINDYc) [11] and more traditional nonlinear system identification technique—regression to linear parameter-varying (LPV) system, whose scheduling parameters are to be identified. These methods allow to construct parsimonious and explainable models of the system dynamics, capturing

*M.Sc. Student, Faculty of Aerospace Engineering, Delft University of Technology, abeno@tudelft.nl.
†Assistant Professor, Faculty of Aerospace Engineering, Delft University of Technology, j.sodja@tudelft.nl.
‡Assistant Professor, Faculty of Aerospace Engineering, Delft University of Technology, x.wang-6@tudelft.nl.

*In fact, there is potential for nearly instantaneous actuation by using ram air to rotate the SVGs around an axis slightly offset from its geometric center.

Fig. 1 Concept design of a switchable vortex generator: (A) position of minimum impact on drag for nominal cruise conditions; (B) vortex generation to suppress/delay separation at high angles of attack and low speeds; (C) spoiler configuration causing massive airflow separation for gust load alleviation.

the underlying physics on low-dimensional manifolds in a feature space. Our approach emphasizes transparency and interpretability, aiming to map system dynamics to well-known flow coherent structures, such as an attached vortex or massive flow separation. This strategy not only allows the discovery of underlying physical phenomena in actuated systems but also informs an iterative design process.

To better understand the justification of the proposed methodology, we first define what model explainability means within the scope of this work. Most notably, sparsity does not necessarily imply explainability. Strictly following Occam's-razor principles may still lead to lack of transparency. Even SINDYc framework depends on hyperparameter tuning, such as the choice of sparsity-promoting algorithms (e.g., least absolute shrinkage and selection operator (LASSO) [12], sequentially thresholded least squares (STLSQ) [13], model selection along Pareto front using an information criterion, such as Akaike information criterion (AIC) [14, 15] or Bayesian information criterion (BIC) [16]), or the choice of the type of identified dynamics—explicit vs. implicit [17]. Our data-driven models rely exclusively on feature vector consisting of quantities (coefficients of lift and moment) which can be estimated from typical sensor measurements. Current state-of-the-art explainable data-driven methods on aeroelastic modeling rely on data-driven adjustments to analytical solutions, such as the Theodorsen's solution [2, 3]. Fully black-box models traditionally use convolutional autoencoders to obtain system dynamics in the latent space using, e.g., SINDY [18], leading to very low dimensional latent space, but lack interpretability. Control of aeroelastic structures with morphing wing has been attempted using dynamic mode decomposition with control (DMDc) [19, 20], but without any actuator-disturbance coupling. Lastly, [21] shows that system dynamics for aeroelastic structures can be embedded in time-delay coordinates using coefficient of lift, identifying transonic buffet as Stuart-Landau oscillator.

This work envisions several innovations. System identification will depend on dynamics of feature vectors which consist from integral quantities (lift and moment) and structural states, as inspired by [10]. Physical interpretability will be grounded in aerodynamic coherent structures identified from flowfield snapshots. A significant advantage of this framework is the future potential in discovering new flow physics governing actuator-disturbance interactions. By analyzing how model predictive control (MPC) exploits these interactions, we envision gained insights into potential improvements in the physical actuator design. Furthermore, the use of sensors measuring upstream flow conditions to detect disturbances before they reach wings facilitates anticipative rather than reactive control strategies.

This paper is structured as follows. Firstly, setup of the computational fluid dynamics (CFD) simulations is described in section II. This includes the description of mesh requirements and generation, modeling of structural aeroelastic effects and fluid-structure interaction (FSI) solver strategy. Secondly, section III introduces system identification of wing-gust and wing-SVG systems using SINDYc and LPV systems, respectively. Attention is paid to system-theoretic mapping of dynamic phenomena associated with aerodynamic loads on the wing with coherent flow structures found in flow snapshots.

II. Simulation Setup

As one of the main objectives of this study is to evaluate the effectiveness of SVGs for gust load alleviation, the aircraft is not modeled in its entirety due to prohibitive computational costs; instead, the analysis focuses on a simplified wing geometry obtained as a straight extrusion of the NASA Whitcomb integral supercritical airfoil [22]. The dimensions of the wing extrusion and flow conditions employed in this study are derived from the operational parameters

of the short-medium range DLR-F25 research baseline aircraft [23], derived from the Airbus A321 platform. All CFD simulations correspond to the aircraft's nominal approach condition at sea-level, international standard atmosphere. The SVG geometry and placement follow an effective configuration from earlier investigation in [8]. The aerodynamic analyses were performed using three-dimensional, unsteady, incompressible RANS CFD simulations with a deforming mesh to accommodate wing's heave and pitch degrees of freedom, as well as an overset mesh to accommodate SVG rotation. All simulations were conducted with the Ansys Fluent solver. Mesh was generated using Ansys Workbench Meshing and Ansys ICEM CFD.

A. Geometry and Flow Conditions

The geometric properties of the wing and SVG are based on the requirement of $\phi = 50\%$ wall ratio [8], which is defined as the ratio of the SVG length and the distance between the rotation axes of two adjacent SVGs. Hence, when the SVGs are rotated perpendicular to the incoming flow, and the wing is assumed to have SVGs placed periodically next to each other throughout the span of the wing, the wall ratio corresponds to the overall fraction of the wingspan blocked by the SVGs. Simulating the entire wing would, however, be too computationally expensive within the scope of this study. Thus, only representative section of the wing is simulated with periodic boundary conditions on the sides. This wing section is assumed to be straight extrusion of the local wing profile defined by the NASA Whitcomb integral supercritical airfoil, with one SVG positioned in the middle of the section span and at 25% chord. This can be seen in Figure 2. Detailed overview of the geometry is given in Table 1.

Table 1 Geometric properties of the extruded wing and SVG. Entries $Position_{direction}$ denote the SVG position along this *direction* defined by the wing geometry.

Wing		SVG			
Chord [m]	Span [m]	Height [m]	Length [m]	$\text{Position}_{\text{Chord}}$ [m]	$\text{Position}_{\text{Span}}$ [m]
$\text{MAC}_{\text{DLR F25}}$	0.2c	0.04c	0.08c	25%	50%
3.54	0.708	0.142	0.283	0.885	0.354

The undisturbed airflow properties correspond to the nominal approach conditions of the DLR-F25 aircraft at sea level height, international standard atmosphere, and are summarized in Table 2. The flow is assumed unsteady and incompressible. Although the assumption on incompressibility does not hold in the vicinity of the SVG (especially at high angles of rotation), the authors found this assumption much stabilizing in terms of the solver convergence. This motivates further research on developing unified CFD frameworks for low-speed compressible solvers. As such, the flow is solved with URANS equations and standard $k-\omega$ SST turbulence model [24]. The inflow and outflow boundary conditions are Ansys Fluent's *velocity inlet* and *pressure outlet*, respectively, while the sides mimic periodicity along wing span with periodic boundary conditions. The wing possesses wall-no-slip boundary condition, but the SVG possesses wall-slip (zero shear at the SVG wall) boundary condition, in order to alleviate stringent requirements on boundary layer resolution near the wall (see Figure 2). The spatial discretization is 2^{nd} order and temporal discretization is implicit 2^{nd} order. The time-resolved simulations are started from the initial condition of the corresponding fully converged steady-state solution.

Table 2 Undisturbed airflow properties in nominal approach conditions for DLR-F25 aircraft at sea level height, international standard atmosphere.

Density [kg/m^3]	Dynamic viscosity [kg/(m s)]	Freestream velocity [m/s]	Reynolds number [-]
1.225	$1.81 \cdot 10^{-5}$	70.0	$16.8 \cdot 10^{6}$

Mesh consists of three fundamentally different regions: deforming mesh comprising most of the computational domain, rigid mesh in the immediate vicinity of the wing and overset mesh embedding the SVG, see Figure 2. Firstly, the deforming mesh accommodates movement of the wing in heave and pitch degrees of freedom using radial-basis-function smoothing. Secondly, the mesh in the near vicinity of the wing moves rigidly with the wing in order to preserve boundary layer resolution of $y^+ \leq 1$ when the SVG is rotated parallel with the incoming freestream. Lastly, the center of the SVG overset mesh moves rigidly with the wing, but it is allowed to rotate along an axis perpendicular to the

wing. The cell growth in the wing-normal direction mimics the boundary layer cell growth of the background mesh. Unfortunately, the overset mesh could not have been placed directly on top of the wing. Thus, there is 1 [mm] gap between the wing wall and the SVG. In reality, the SVG would start at the wing surface.

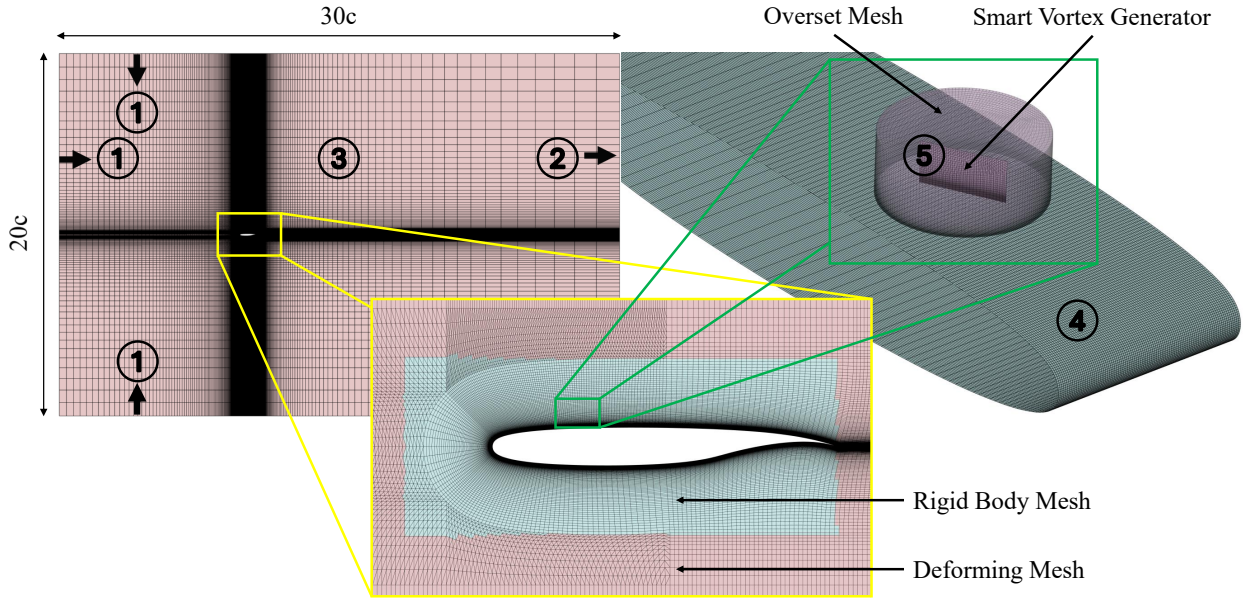

Fig. 2 Hexahedral mesh of the computational domain and detailed view of the SVG overset mesh. Numbers specify boundary conditions in the following order: 1=Velocity Inlet, 2=Pressure Outlet, 3=Periodic, 4=Wall-No-Slip, 5=Wall-Slip. The mesh in the immediate vicinity of the wing moves rigidly with the wing (in order to preserve boundary layer resolution), while the surrounding mesh deforms to accommodate the movement in heave and pitch degrees of freedom. SVG is embedded as an infinitely thin surface within the SVG overset mesh, which follows the movement of the wing while being allowed to rotate around an axis perpendicular to the wing surface.

B. Aeroelasticity and FSI Coupling

The wing is allowed motion in two degrees of freedom: heave and pitch. The structural dynamics is approximated by mass-damper-spring system in both degrees of freedom. Gravitational force has also been taken into consideration. The coupled equations of motion are given in non-dimensionalized form in Equation 1. The more compact notation is introduced in Equation 2, where the structural state is denoted with $\boldsymbol{x}_\mathrm{s} = \left[\frac{h}{b}, \theta\right]^\top$. The forcing of the mass-damper-spring system is defined based on the difference of unsteady ($F_\mathrm{aero}, M_\mathrm{aero}$) and steady-state aerodynamic loads ($F^0_\mathrm{aero}, M^0_\mathrm{aero}$). Equation 1 corresponds to the free-body diagram in Figure 3a.

$$\begin{bmatrix} 1 & \cos(\theta)x_\theta \\ \cos(\theta)x_\theta & r^2 \end{bmatrix} \begin{bmatrix} \frac{\ddot{h}}{b} \\ \ddot{\theta} \end{bmatrix} + \begin{bmatrix} 2\zeta_h\omega_h & 0 \\ 0 & 2\zeta_\theta\omega_\theta r^2 \end{bmatrix} \begin{bmatrix} \frac{\dot{h}}{b} \\ \dot{\theta} \end{bmatrix} + \begin{bmatrix} \omega_h^2 & 0 \\ 0 & \omega_\theta^2 r^2 \end{bmatrix} \begin{bmatrix} \frac{h}{b} \\ \theta \end{bmatrix} = \begin{bmatrix} \frac{F_\mathrm{aero} - F^0_\mathrm{aero}}{mb} + \sin(\theta)x_\theta\dot{\theta}^2 \\ \frac{M_\mathrm{aero} - M^0_\mathrm{aero}}{mb^2} + \frac{g}{b}x_\theta\,(1 - \cos(\theta)) \end{bmatrix} \quad (1)$$

$$\boldsymbol{M}\ddot{\boldsymbol{x}}_\mathrm{s} + \boldsymbol{C}\dot{\boldsymbol{x}}_\mathrm{s} + \boldsymbol{K}\boldsymbol{x}_\mathrm{s} = \boldsymbol{f} \quad (2)$$

It must be noted that the natural frequencies ω and damping ratios ζ present in Equation 1 correspond to the decoupled system, which is defined by the fictitious situation in which the center of mass and center of aeroelasticity coincide, in which case the static unbalance parameter equals to $x_\theta = 0$. In fact, the system defined in Equation 1 is nonlinear, hence, there is no notion of discrete eigenfrequency spectrum. The equations of motion have been implemented in CFD code in their fully nonlinear form, however, simulations later show that the wing operates in the strictly linear region, which can be approximated by $\theta \approx 0$. As such, the eigenfrequencies of the linearized system can be easily found with the ansatz of $\boldsymbol{x}_\mathrm{s} = \boldsymbol{u}e^{\lambda t}$, where $\boldsymbol{u}$ stands for mode shape. Equation 2 however cannot be solved by

modal analysis, and the natural frequencies are most easily obtained numerically as the eigenvalues of the system matrix $\boldsymbol{A}$ defined in Equation 3.

$$\boldsymbol{A} = \begin{bmatrix} \mathbf{0} & \boldsymbol{I} \\ -\boldsymbol{M}^{-1}\boldsymbol{K} & -\boldsymbol{M}^{-1}\boldsymbol{C} \end{bmatrix} \tag{3}$$

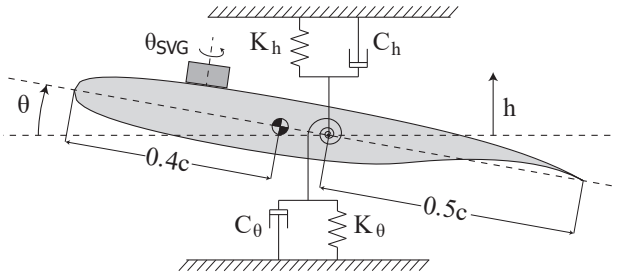

(a) Diagram of the relative position of the center of mass (40% chord) and aeroelastic center (50% chord). The wing moves in heave and pitch degrees of freedom. The structural dynamics is approximated with mass-damper-spring system for both degrees of freedom.

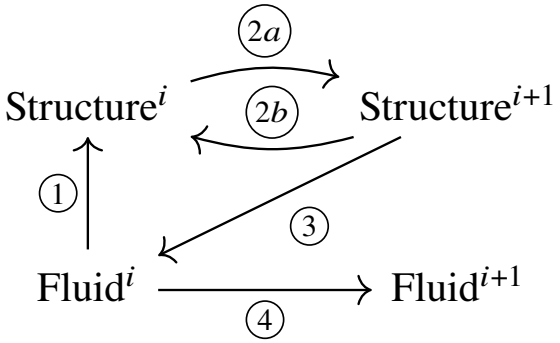

(b) Diagram of the FSI coupling. Firstly, the structure converges on its position for the time-step $i+1$ based on the aerodynamic forces corresponding to time-step i and external forces corresponding to time-step $i+1$. The fluid is then solved based on the newly deformed mesh.

Fig. 3 Overview of the aeroelastic system and the coupling of fluid and structural solver within FSI framework.

The coupled frequencies stemming from Equation 3 can be selected arbitrarily by carefully tuning the decoupled-system natural frequencies and damping ratios ω and ζ. The parameters chosen for the simulations throughout this study are given in Table 3. The fluid-structure coupling within CFD is depicted in Figure 3b. The FSI algorithm follows loose coupling. Firstly, it converges on new mesh deformation based on the aerodynamical forces computed for time-step i and external forces computed for time-step $i+1$ (mimicking implicit scheme). Secondly, it computes the flow field corresponding to the newly deformed mesh. However, there is no feedback from the fluid solver to the structural solver to enforce strong FSI coupling. This discrepancy in correspondence between fluid state and structural state has been addressed with simulation time-step based on Courant–Friedrichs–Lewy (CFL) number; CFL ≈ 2.

Table 3 Parameters of the aeroelastic system defined by system matrix $\boldsymbol{A}$ in Equation 3.

λ_h [-]	λ_θ [-]	$f_h{}^*$[1/s]	$f_\theta{}^*$[1/s]	ζ_h [-]	ζ_θ [-]
-0.619 ± 31.3i	-2.95 ± 134i	4.98	21.4	0.0185	0.0220
x_θ [-]	r^2 [-]	m [kg]	g [m/s^2]	C_L^0 [-]	C_M^0 [-]
0.200	0.333	50.0	9.81	0.476	-0.0171

* This is the (coupled) damped frequency.

C. Simulating Wind Gusts

Wind gust is localized, sudden and brief increase in wind speed. As [25] describes, the formation of wind gusts depends on a variety of conditions, such as friction, pressure changes and local thermal effects. Distinction must be made between wind gusts and turbulence. Turbulence should be thought of as a random process of high frequency, numberless and chaotic eddies of various sizes superimposed on a mean velocity profile. Unlike turbulence, according to [26], wind gusts usually last for few seconds before they drop below some threshold level. Thus, they are coherent structures, although, their occurrence may still be better thought of as probabilistic in nature.

The scope of this work, however, is limited to simulating deterministic gusts of prescribed shape. This simplification of the actual phenomenon is in accordance with the certification process, as stipulated in [27]. An encounter with an idealized wind gust is depicted in Figure 4. The discrete prescribed wind gust is superimposed on the ambient stationary air. Shape of the wind gust considered in this work is the discrete *1-cos* wind gust, stipulated by EASA [27], defined in Equation 4, with gust amplitude $A_g = 7.62$ [m/s], stipulated for certification at approach conditions. This rise in incoming vertical velocity of the ambient freestream airflow results in apparent increase of the angle of attack $\Delta\alpha_{AOA} \approx 6.21$ [deg].

$$u_g = \begin{cases} 0, & s < 0 \\ \frac{A_g}{2}\left[1 - \cos\left(\frac{\pi s}{H_g}\right)\right], & 0 \le s \le 2H_g \\ 0, & s > 2H_g \end{cases} \tag{4}$$

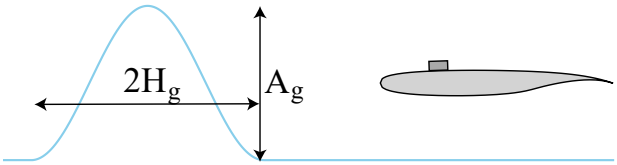

Fig. 4 Encounter with discrete 1-cos wind gust. The blue line depicts increase in vertical velocity of the freestream airflow, representing the wind gust.

The idealized wind gusts can be incorporated into CFD simulations with varying degree of physical realism, depending on the available computational resources. This is achieved either through modification of the boundary conditions, modification of the governing equations, or a combination of both. In this work, we resort to the most physically rigorous way of incorporating wind gusts in CFD simulations — Resolved Atmosphere Approach (RAA).

RAA introduces wind gusts through far-field inlet boundaries of the computational domain. The boundary conditions are modified by superimposing the gust velocity on the freestream velocity. The far-field boundary condition thus becomes function of time and space, as the gust travels downstream with the freestream velocity. This is usually also the easiest to implement in any general-purpose commercial CFD code, such as Ansys Fluent[†]. The only disadvantage of RAA is that the mesh must be very fine throughout the entire computational domain in order to accommodate the advection of the gust without much numerical dissipation.

III. System Identification

The system identification process concerns identifying the effect of gust and SVG motion on the aerodynamic loads acting on the wing. Hence, function of the form given in Equation 5 must be identified. It must be noted that we ultimately seek expression for $\Delta\dot{C}_{L,M}$, instead of $\Delta C_{L,M}$ for better capturing the dynamic properties.

$$\begin{bmatrix} \Delta\dot{C}_L \\ \Delta\dot{C}_M \end{bmatrix} = \boldsymbol{f}(\dot{u}_g, \dot{\theta}_{\text{SVG}}, \boldsymbol{x}_{\text{internal}}) \tag{5}$$

Here, $\boldsymbol{x}_{\text{internal}}$ denotes the hidden states, also called aerodynamic states, which correspond to the memory of the system. The wing-gust and wing-SVG systems are first identified separately. This is motivated by the fact that within this study the wing under gust excitation never enters nonlinear regime, such as stall or flutter (at least withing the scope of this study).

A. Identification of Wing-Gust System

In the spirit of sparse identification of nonlinear dynamics with control (SINDYc) [11, 13], the aim here is at constructing feature library of explanatory variables (e.g., motion in heave and pitch degrees of freedom, gust velocity) which can be regressed to the response variables ($\Delta\dot{C}_L$ and $\Delta\dot{C}_M$). This is motivated by the availability of the many potential-theory-based models (later also used as explanatory variables) of unsteady aerodynamic loads, such as the lift response due to an incoming step gust and step changes in angle of attack, modeled by Küssner [30] and Wagner [30] step-response functions, respectively. These potential-theory-based models provide perfect candidates for the feature

[†]An attempt was also made at simulating wind gusts with an overset transport mesh method [28] and split velocity method [29], unfortunately, Ansys Fluent could not handle the interpolation process between overset mesh and the background mesh for large structured overset meshes (for which it also does not allow using periodic boundary conditions) and it lacks boundary condition permitting specified velocity normal to wall surface, respectively.

library basis functions. It is the SINDYc algorithm which should select the combined model which best explains the measured $\Delta\dot{C}_L$ and $\Delta\dot{C}_M$ dynamics, as any one model might individually lack the immediate generalizability to the real viscous flow. Moreover, interaction terms and higher order nonlinear terms constructed from the potential-theory-based basis functions can be included in the feature library to allow representing nonlinear phenomena, if present.

The SINDY and SINDYc algorithms are best described in [11, 13], but are also briefly introduced here for the sake of completeness. SINDYc is purely data-driven algorithm which only relies on collecting measurements of the studied system, which is assumed to be given by Equation 6.

$$\dot{\boldsymbol{x}} = \boldsymbol{f}(\boldsymbol{x}, \boldsymbol{u}) \tag{6}$$

The collected states $\boldsymbol{x}_k = \boldsymbol{x}(k\Delta T)$, their time derivatives $\dot{\boldsymbol{x}}_k = \dot{\boldsymbol{x}}(k\Delta T)$ and control inputs $\boldsymbol{u}_k = \boldsymbol{u}(k\Delta T)$ are arranged into three data matrices, given in Equation 7.

$$\boldsymbol{X} = \begin{bmatrix} | & | & & | \\ \boldsymbol{x}_1 & \boldsymbol{x}_2 & \dots & \boldsymbol{x}_m \\ | & | & & | \end{bmatrix} \qquad \dot{\boldsymbol{X}} = \begin{bmatrix} | & | & & | \\ \dot{\boldsymbol{x}}_1 & \dot{\boldsymbol{x}}_2 & \dots & \dot{\boldsymbol{x}}_m \\ | & | & & | \end{bmatrix} \qquad \boldsymbol{\Upsilon} = \begin{bmatrix} | & | & & | \\ \boldsymbol{u}_1 & \boldsymbol{u}_2 & \dots & \boldsymbol{u}_m \\ | & | & & | \end{bmatrix} \tag{7}$$

The feature library Θ, given in Equation 8, of generally nonlinear functions can then be constructed based on $\boldsymbol{X}$ and $\boldsymbol{\Upsilon}$.

$$\Theta^\top(\boldsymbol{X}, \boldsymbol{\Upsilon}) = \begin{bmatrix} \text{———} & \mathbf{1} & \text{———} \\ \text{———} & \boldsymbol{X} & \text{———} \\ \text{———} & \boldsymbol{X}^2 & \text{———} \\ \text{———} & \sin(\boldsymbol{\Upsilon}\boldsymbol{X}) & \text{———} \\ \text{———} & \boldsymbol{\Upsilon}^2 & \text{———} \\ & \vdots & \end{bmatrix} \tag{8}$$

The main task of SINDYc is to solve the regression problem $\dot{\boldsymbol{X}} = \Xi\Theta^\top(\boldsymbol{X}, \boldsymbol{\Upsilon})$, while promoting sparsity in the solution. The default choice for the sparsity promoting optimizer is the sequentially thresholded least squares algorithm (STLSQ). In general, STLSQ attempts to minimize the objective function given in Equation 9, by repeatedly performing the regression until convergence, eliminating candidate functions in Θ whose weight in the weight matrix Ξ falls below specified threshold, θ_{STLSQ}. Of course, the regression problem is unbiased at convergence by removing the regularization term. This leaves two hyperparameters to be tuned — θ_{STLSQ} and α.

$$\|\dot{\boldsymbol{X}} - \Xi\Theta^\top(\boldsymbol{X}, \boldsymbol{\Upsilon})\|_2^2 + \alpha\|\Xi\|_2^2 \tag{9}$$

Models produced by STLSQ for various values of θ_{STLSQ} and α can be rated with the Akaike information criterion (AIC) [16, 31] to aid model selection. AIC is well-established model selection criterion and it is derived from the Kullback-Leibler divergence of the true probability density function generating the data and the approximating probability density function. It was shown by Akaike that this choice leads to the penalized log-likelihood information criterion, given in Equation 10. As such, AIC is based on the log-likelihood of the estimator of the true probability density function generating the data and penalizes the number of independently adjusted parameters d of this estimator. It thus balances the dimensionality of the identified model and how well it fits the measurements.

$$AIC = -2\log(\text{Maximum Likelihood}) + 2d \tag{10}$$

A modified version of the above AIC will be used for the purposes of this study, adjusting for the continuous time domain of the regressed signals. This modified version is similar to the one proposed in [32], and is given in Equation 11. Here, $\boldsymbol{x}_i(t)$ is the exact system state obtained from CFD data and $\hat{\boldsymbol{x}}_i(t)$ is its approximation based on SINDYc-AIC-chosen model, d is then the number of non-zero entries in Ξ. Subscript i denotes simulation index. Many simulations were conducted with different gusts in order to excite the system enough to prevent ill-posedness of the regression problem[‡].

[‡]Another approach to system identification would be to prescribe wing movement instead of leaving this to the structural dynamics solver. This method would allow to purposefully prescribe orthogonal explanatory signals, making the regression problem better conditioned. However, meticulous attention must then be paid in order to guarantee sufficient smoothness of the explanatory signal, such that higher order derivatives, if needed, are continuous. Moreover, observing system under natural excitation is the more common situation, hence this approach was chosen for this study.

$$\widehat{\mathrm{AIC}} = 2\log\left(\frac{1}{N}\sum_{i=1}^{N}\frac{\int|\boldsymbol{x}_i(t)-\hat{\boldsymbol{x}}_i(t)|^2\,dt}{\int|\boldsymbol{x}_i(t)|^2\,dt}\right)+2d \tag{11}$$

The chosen system state variables $\boldsymbol{x}$ and control inputs $\boldsymbol{u}$ are given in Equation 12 and Equation 13. There is no need to re-identify the approximate structural dynamics given by the structural system matrix in Equation 3, and thus the structural states are supplied to the SINDYc framework as a control signal. h_{Wagner} and $h_{\text{Küssner}}$ are the impulse response functions corresponding to the widely used Bisplinghoff's approximation of the Wagner and Küssner step response functions [30]. They are based on potential theory and represent the time-lagged aerodynamic effects — system memory. The combination of such chosen basis functions guarantees explainability of the selected model, while STLSQ guarantees sparsity.

$$\boldsymbol{x} = [\Delta C_L, \Delta C_M]^\top \tag{12}$$

$$\boldsymbol{u} = \left[\dot{\theta}, \frac{\ddot{h}}{b}, \ddot{\theta}, \dot{z}_{\mathrm{W}}(\theta), \dot{z}_{\mathrm{W}}\left(\frac{\dot{h}}{b}\right), \dot{z}_{\mathrm{W}}(\dot{\theta}), \frac{\dot{u}_{\mathrm{g}}}{u_\infty}, \dot{z}_{\mathrm{K}}\left(\frac{u_{\mathrm{g}}}{u_\infty}\right), \right]^\top \qquad \begin{cases} z_{\mathrm{W}}(y) = y * h_{\text{Wagner}} \\ z_{\mathrm{K}}(y) = y * h_{\text{Küssner}} \end{cases} \tag{13}$$

Both positive, $+u_{\mathrm{g}}$, and negative, $-u_{\mathrm{g}}$, gusts were simulated for the purposes of system identification. Their reduced frequency, $k = \frac{\pi b}{H}$, and half span, H, are listed in Table 4. *Training* was performed using two-fold stratified cross-validation with 87% of the data used for training and 13% of the data used for evaluation. It is the evaluation data set for which the $\widehat{\mathrm{AIC}}$ was computed. The stratification was based on the sign of the gust ($\pm u_{\mathrm{g}}$) and reduced frequency k. Class membership to low frequency gusts class was determined based on $k \leq 0.4$, case otherwise belonged to the high frequency gusts class. It is customary to use $k = 0.2$ as the demarcation line between unsteady and quasi-steady aerodynamics, but examination of the data revealed onset of well-defined oscillatory behavior at $k = 0.4$. Several definitions of Θ were examined — up to 2^{nd} order polynomials in $\boldsymbol{X}$ and $\boldsymbol{\Upsilon}$, including cross-terms — but it is clear that no such nonlinearities are present in the datasets. This is mostly due to the choice of the wing mass which prohibits large deflections due to its high inertia. The table of $\widehat{\mathrm{AIC}}$s depending on the value of hyperparameters θ_{STLSQ} and α is given in Figure 5, corresponding to the simple case of $\Theta^\top(\boldsymbol{X}, \boldsymbol{\Upsilon}) = \begin{bmatrix} \boldsymbol{X} \\ \boldsymbol{\Upsilon} \end{bmatrix}$.

Table 4 Simulation design matrix. Simulations were conducted using discrete 1-cos gusts of reduced frequency k, equivalently expressed using the gust half-span H, for both positive, $+u_{\mathrm{g}}$, and negative, $-u_{\mathrm{g}}$ cases.

k [-]	0.05	0.1	0.2	0.4	0.6	0.8	1	2
H [m]	111	55.6	27.8	13.9	9.27	6.95	5.56	2.78

Based on the results in Figure 5, the model with the lowest $\widehat{\mathrm{AIC}}$ is chosen as the model which best balances sparsity with data fit. For comparison, Equation 14 and Equation 16 provide the identified Ξ for the lowest $\widehat{\mathrm{AIC}}$ model and an overfit model—which makes use of all of the available explanatory variables, respectively.

$$\begin{bmatrix} \Delta\dot{C}_L \\ \Delta\dot{C}_M \end{bmatrix} = \begin{bmatrix} -0.0992\frac{\ddot{h}}{b} + 6.21\dot{z}_{\mathrm{K}}\left(\frac{u_{\mathrm{g}}}{u_\infty}\right) \\ -0.0485\dot{z}_{\mathrm{W}}\left(\frac{\dot{h}}{b}\right) + 1.64\dot{z}_{\mathrm{K}}\left(\frac{u_{\mathrm{g}}}{u_\infty}\right) \end{bmatrix}_{\min\left(\widehat{\mathrm{AIC}}\right)} \tag{14}$$

Upon closer examination of the identified coefficients, the minimum $\widehat{\mathrm{AIC}}$ model identified in Equation 14 shows significant similarity with unsteady potential theory. When only considering the basis functions chosen by the STLSQ optimization algorithm, quasi-steady potential flow defines the aerodynamic loads as given in Equation 15, [30]. The identified coefficients within the minimum $\widehat{\mathrm{AIC}}$ model resemble their quasi-steady potential theory counterparts.

$$\Delta\dot{C}_L = -\frac{2\pi b}{u_\infty}\frac{\ddot{h}}{b} + 2\pi\dot{\theta} = -0.159\frac{\ddot{h}}{b} + 6.28\dot{\theta} \tag{15}$$

However, the coefficients identified for the overfit model given in Equation 16 do not directly correspond to the unsteady potential theory. This is because many of the physically unique terms (e.g., linear acceleration in heave or

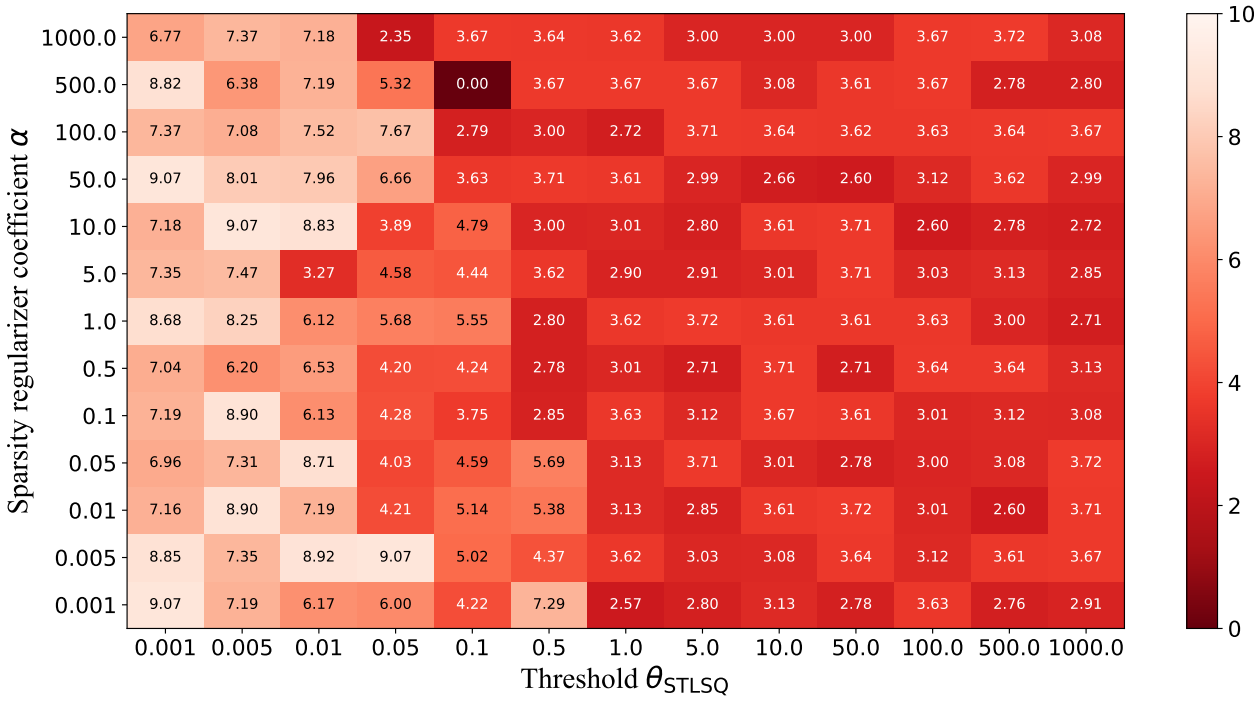

Fig. 5 $\Delta\widehat{\mathrm{AIC}}$ computed for the evaluation dataset, corresponding to the hyperparameters θ_{STLSQ} and α of the STLSQ optimizer. $\Delta\widehat{\mathrm{AIC}}$ is defined as the relative score with respect to the lowest identified one, such that $\Delta\widehat{\mathrm{AIC}} = \widehat{\mathrm{AIC}} - \min\left(\widehat{\mathrm{AIC}}\right)$.

angular velocity in pitch) come together with their time-lagged counterparts defined by convolutions with Wagner and Küssner impulse response functions. Their interpretation should ultimately correspond to feed-through and internal states within linear time-invariant systems. Furthermore, because the overfit model uses all of the candidate basis functions within library Θ, it is also difficult to differentiate between terms contributing unique information and alias terms, which merely happen to correlate with other terms within our training dataset. As such, sparsity promoting optimizer, such as STLSQ, and model selection based on some information criterion (e.g., AIC) also effectively prevent inclusion of aliased terms within generated models. It might seem trivial to use SINDYc methodology, including STLSQ algorithm in combination with an information criterion for model selection, in this case, but it is the first step towards understanding and mainly tuning the definition of such information criterions for cases when the model of the underlying dynamics is truly not known, and neither can it be approximated with (unsteady) potential-flow-based models.

$$\begin{bmatrix}\Delta\dot{C}_L\\ \Delta\dot{C}_M\end{bmatrix} = \begin{bmatrix} 57.8\dot{\theta} - 0.241\frac{\ddot{h}}{b} + 6.22\ddot{\theta} - 14.6\dot{z}_{\mathrm{W}}(\theta) + 0.332\dot{z}_{\mathrm{W}}\left(\frac{\dot{h}}{b}\right) - 12.2\dot{z}_{\mathrm{W}}(\dot{\theta}) + 0.733\frac{\dot{u}_{\mathrm{g}}}{u_\infty} + 3.827\dot{z}_{\mathrm{K}}\left(\frac{u_{\mathrm{g}}}{u_\infty}\right) \\ 2.87\dot{\theta} + 0.00664\frac{\ddot{h}}{b} + 0.162\ddot{\theta} + 5.16\dot{z}_{\mathrm{W}}(\theta) - 0.0490\dot{z}_{\mathrm{W}}\left(\frac{\dot{h}}{b}\right) - 0.329\dot{z}_{\mathrm{W}}(\dot{\theta}) + 0.190\frac{\dot{u}_{\mathrm{g}}}{u_\infty} + 1.08\dot{z}_{\mathrm{K}}(\frac{u_{\mathrm{g}}}{u_\infty}) \end{bmatrix} \tag{16}$$

Predictions of the two models for the aerodynamic loads and their derivatives are given in Figure 6a and Figure 6b for the model with minimum $\widehat{\mathrm{AIC}}$ and in Figure 7a and Figure 7b for the overfit model, respectively. These time evolutions of the predicted aerodynamic loads are computed within a coupled structural-aerodynamic ROM solver, combining Equation 1 with both of the previously identified aerodynamic models, as an initial value problem with zero initial condition.

It is interesting to note that even highly unsteady gusts, such as gusts defined by $k \geq 0.4$, induce aerodynamical loads which obey LTI system dynamics. This is due to the fact that the chosen gust amplitude of $A_{\mathrm{g}} = 7.62$ [m/s], inducing apparent increase in angle of attack of $\alpha_{\mathrm{AOA}} = 6.21$ [deg], is not enough to cause flow separation, allowing for attached flow throughout the duration of gust presence. This is shown in Figure 8a and Figure 8b for reduced gust frequencies of $k = 0.05$ and $k = 1$, respectively.

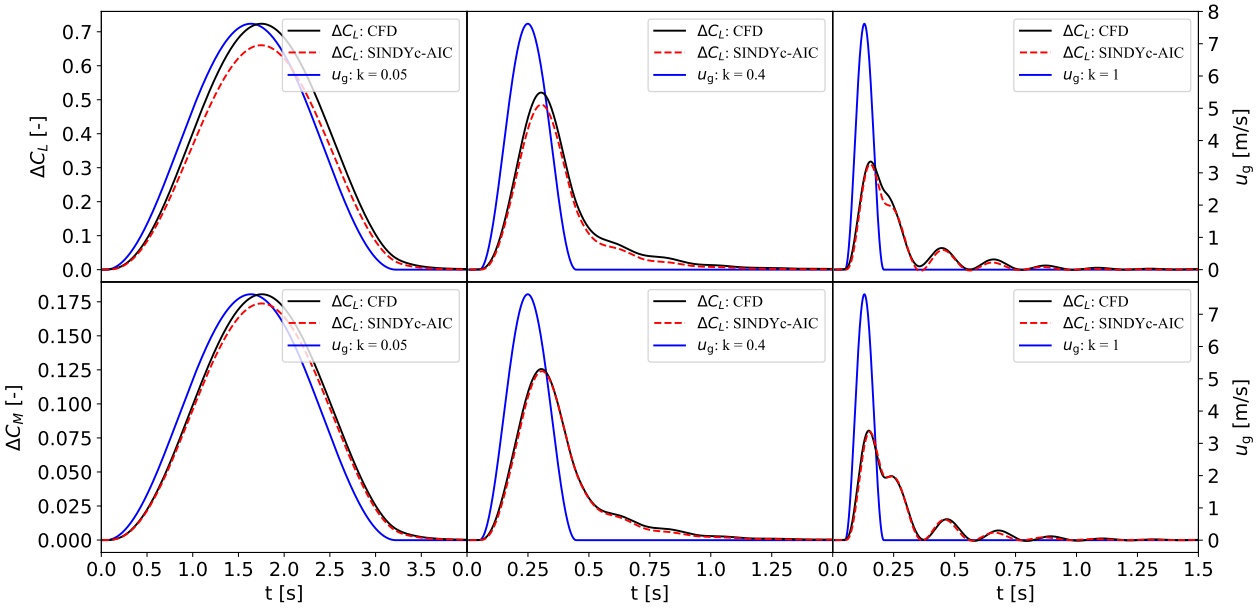

(a) Evolution of the aerodynamic loads due to gust forcing of several reduced frequencies. Comparison of SINDYc-AIC-identified minimum $\widehat{\text{AIC}}$ ROM model with CFD measurements.

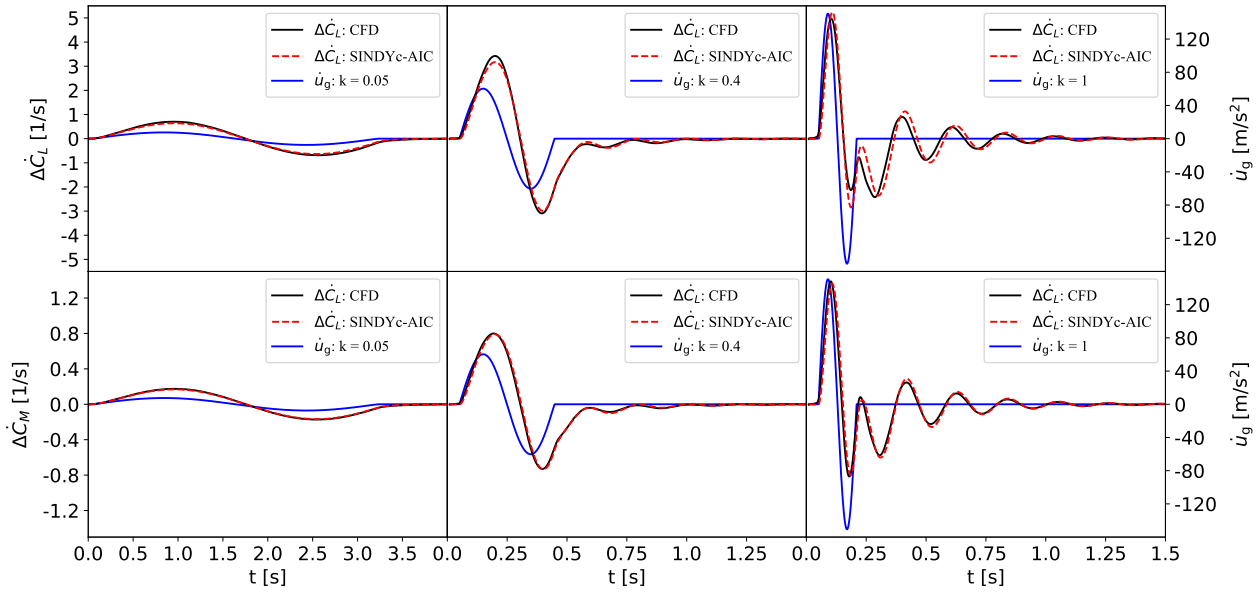

(b) Evolution of the time derivatives of aerodynamic loads due to gust forcing of several reduced frequencies. Comparison of SINDYc-AIC-identified minimum $\widehat{\text{AIC}}$ ROM model with CFD measurements.

Fig. 6 Evolution of the aerodynamic loads due to gust forcing of several reduced frequencies. Comparison of SINDYc-AIC-identified minimum $\widehat{\text{AIC}}$ and overfit ROM models with CFD measurements. ROM predictions were computing using coupled structural-aerodynamic solver with zero initial conditions.

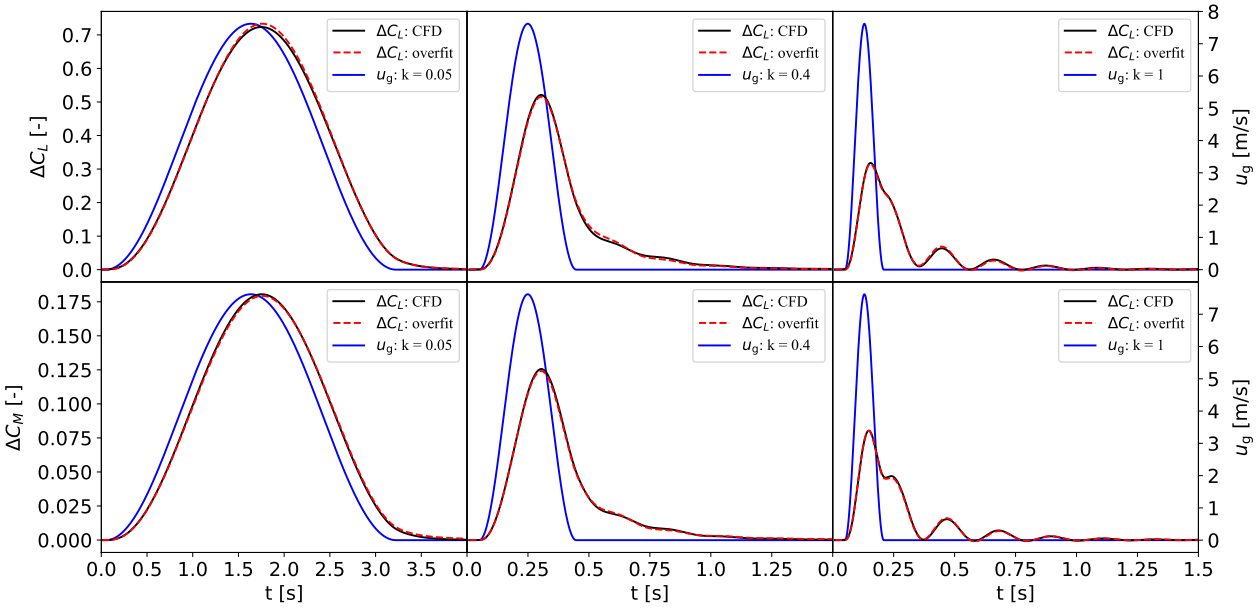

(a) Evolution of the aerodynamic loads due to gust forcing of several reduced frequencies. Comparison of the overfit ROM model with CFD measurements.

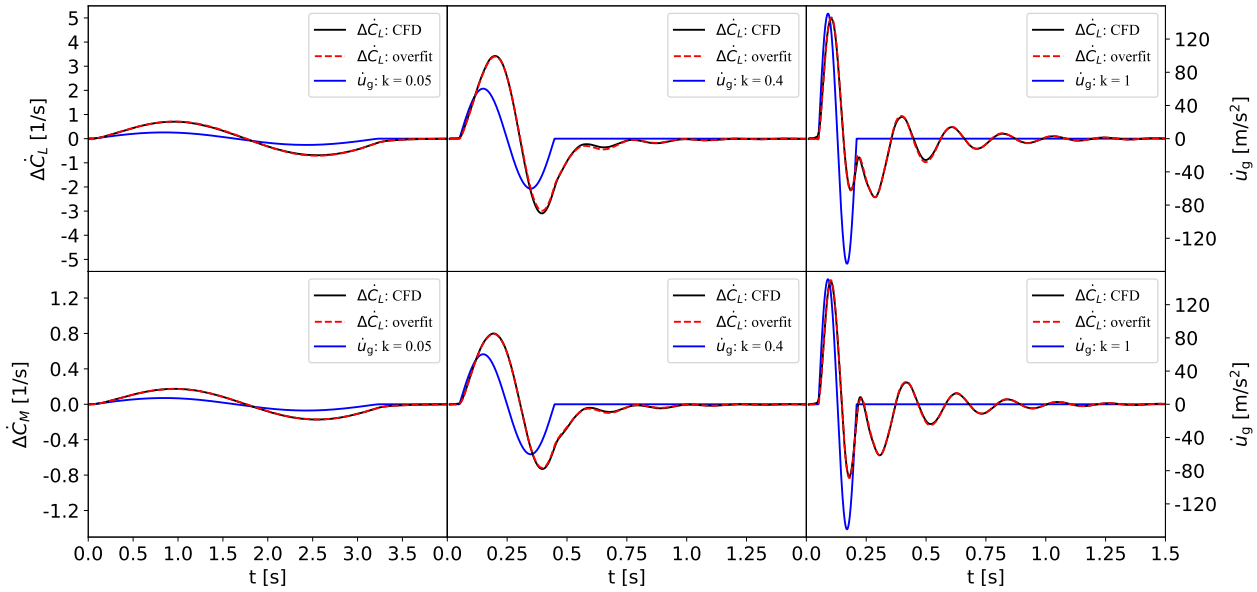

(b) Evolution of the time derivatives of aerodynamic loads due to gust forcing of several reduced frequencies. Comparison of the overfit ROM model with CFD measurements.

Fig. 7 Evolution of the time derivatives of aerodynamic loads due to gust forcing of several reduced frequencies. Comparison of SINDYc-AIC-identified minimum $\widehat{\text{AIC}}$ and overfit ROM models with CFD measurements. ROM predictions were computing using coupled structural-aerodynamic solver with zero initial conditions.

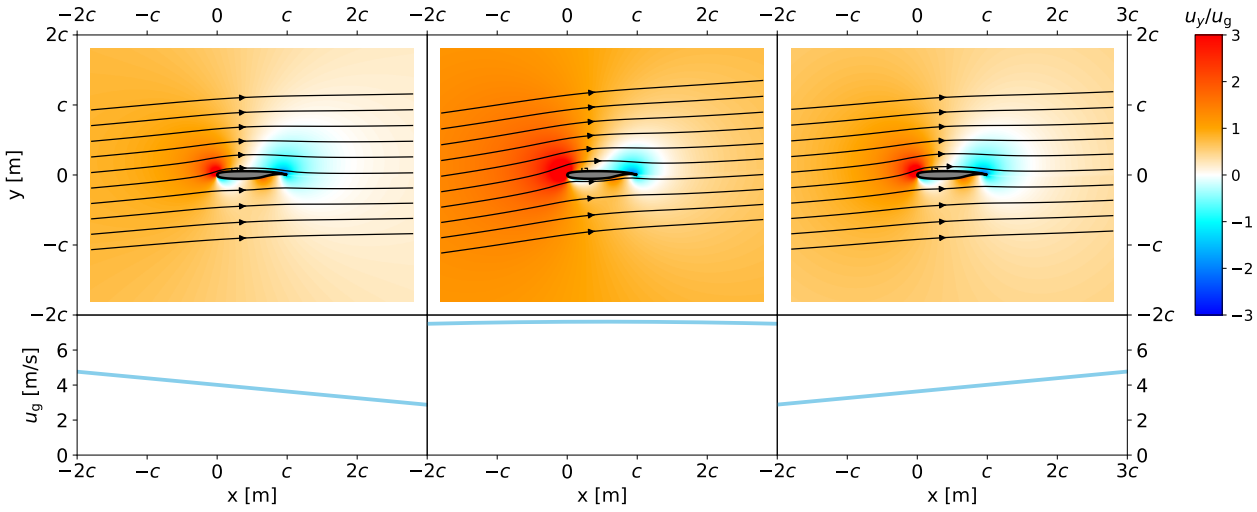

(a) Contour plot of the vertical flow velocity, u_y, superimposed with flow streamlines is shown in the top row. Bottom row shows the spatial distribution of the prescribed gust velocity, corresponding to reduced gust frequency of $k = 0.05$. Every flow snapshot is taken in a reference frame which moves rigidly with the wing.

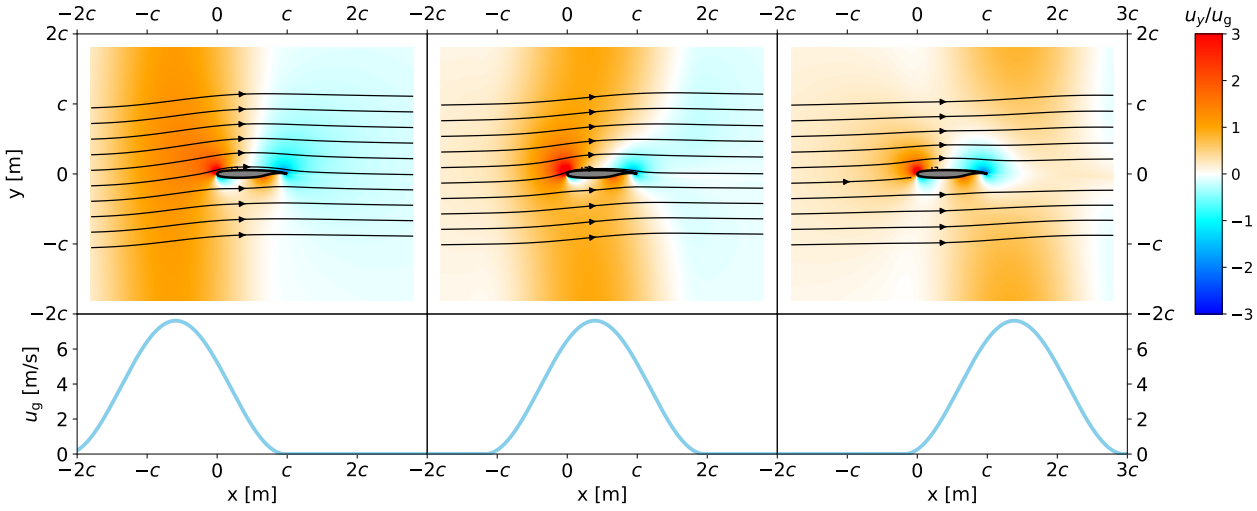

(b) Contour plot of the vertical flow velocity, u_y, superimposed with flow streamlines is shown in the top row. Bottom row shows the spatial distribution of the prescribed gust velocity, corresponding to reduced gust frequency of $k = 1$. Every flow snapshot is taken in a reference frame which moves rigidly with the wing.

Fig. 8 Contour plots of the vertical flow velocity, u_y, superimposed with flow streamlines for wind gusts of reduced frequencies $k = 0.05$ and $k = 1$.

B. Identification of Wing-SVG System

This section addresses the identification of a dynamical model for the wing–SVG system, with emphasis on selecting an appropriate modeling framework given the limitations stemming from the preceding section. In particular, SINDYc is fundamentally a regression algorithm and as such, system memory effects (e.g., system lag with respect to the control input) can be identified in one of two ways. Either the lagged versions of explanatory signals can be supplied to the candidate library of functions Θ, or the higher-order dynamics can be reformulated as first-order systems by augmenting the state and control data matrices with higher-order derivatives. The former approach is inefficient because it requires estimating plausible lags a-priori. The letter relies on access to high-fidelity measurements of higher-order state derivatives, which is especially difficult using experimental data. To overcome these limitations, several alternative nonlinear system identification techniques have been examined.

Autoregressive models (including ARMA, ARMAX, and their nonlinear extension NARMAX [33][§]), are attractive due to their relative ease of implementation and their ability to capture memory effects, by construction. However, these models pose substantial challenges for model-based control, particularly for model-predictive control (MPC), as they require solving and optimizing over delay differential equations. Closely related is the Volterra series solution representation [34], which expresses the solution to nonlinear differential equation as the summation of convolutions of the input signal with Volterra kernels — higher-order counterparts to linear system's impulse response function. However, computing the kernels is not trivial. Moreover, Volterra models are contained within NARMAX models, which serve as a proxy for Volterra kernels. Recurrent neural networks are fundamentally another form of NARMAX models, and data-driven control approaches such as reinforcement learning could possibly inform explicit system identification, but these methods were ultimately deemed unsuitable due to limited interpretability, sparsity and the lack of explicit, physics-informed structure.

Motivated by these considerations, more conventional nonlinear system identification techniques extending upon linear system identification approaches were considered instead. Firstly, the necessity of identifying the type of nonlinearity present in the data was conducted by regressing a linear time-invariant (LTI) system to the data. By assuming that the data originates from an LTI system, it is then possible to use the difference between the true time evolution of aerodynamic loads and its LTI-system approximation to infer the type of nonlinearity[¶]. This is shown in Figure 9. It is clear that the best LTI system which attempts resolving the non-minimum-phase nature of the dynamical system when the SVG is retracted from fully deployed position ($\theta_{\text{SVG}} = 90$ [deg]) to fully retracted position ($\theta_{\text{SVG}} = 0$ [deg]) automatically introduces the same non-minimum-phase dynamics at low SVG rotation angles too. This results in phase and amplitude mismatch between the predicted and true time evolution of the aerodynamic loads for both slowly and fast actuated SVG. This proves that the wing-SVG system is truly non-linear. Specifically, this system does not exhibit any non-minimum-phase behavior for low angles of SVG deployment, but does exhibit non-minimum-phase behavior for high angles of SVG deployment.

Secondly, examination of whether the observed nonlinearity could be attributed to static nonlinear effects in actuation or sensing was conducted before adopting a more general nonlinear model. Formally known as Hammerstein–Wiener models, static nonlinearities include input nonlinearity followed by linear dynamics (Hammerstein model) and linear dynamics followed by nonlinear output (Wiener model). For example, static input nonlinearity could be motivated by the projection of the SVG surface area onto the plane normal to upstream flow streamlines. Polynomial and trigonometric nonlinearities were tested, yielding no improvement in the regression to linear system, suggesting that the dominant nonlinearities truly reside in the system dynamics itself.

These findings motivate the use of Linear Parameter-Varying (LPV) system model, as the next more nonlinear model candidate. General form of an LPV system is given in Equation 17. Although LPV systems are nonlinear in a strict sense, they retain a linear structure whose scheduling parameters, $\boldsymbol{p}(t)$, depend on measurable or estimable variables, rendering them physics-interpretable. The choice of scheduling parameters is not unique and necessarily reflects modeling assumptions. Possible candidates include aerodynamic quantities such as the lift-polar of a flat plate (SVG-like geometry), possibly augmented with memory effects (e.g., via Wagner or Küssner type of aerodynamic lag), or discrete regime indicators encoding flow states around the SVG, such as fully separated or vortex-attached conditions. Despite this arbitrariness, LPV models provide a structured compromise between fidelity and interpretability, allowing

[§]Autoregressive models are usually considered in the discrete-time system identification but their continuous-time counterparts can easily be constructed by selecting appropriate sampling period.

[¶]Other data-driven system identification techniques can be used to construct the linear system approximation of the nonlinear system. Specifically, Observer Kalman Filter Identification (OKID) [35] method followed by the Eigensystem Realization Algorithm (ERA) [36] can be used to identify the linear system impulse response function. At the same time, control over the number of leading singular values in the approximation of the data-driven Hankel matrix allows for reduced-order modeling of the linear system, leaving more space to infer the type of nonlinearity present in the original data.

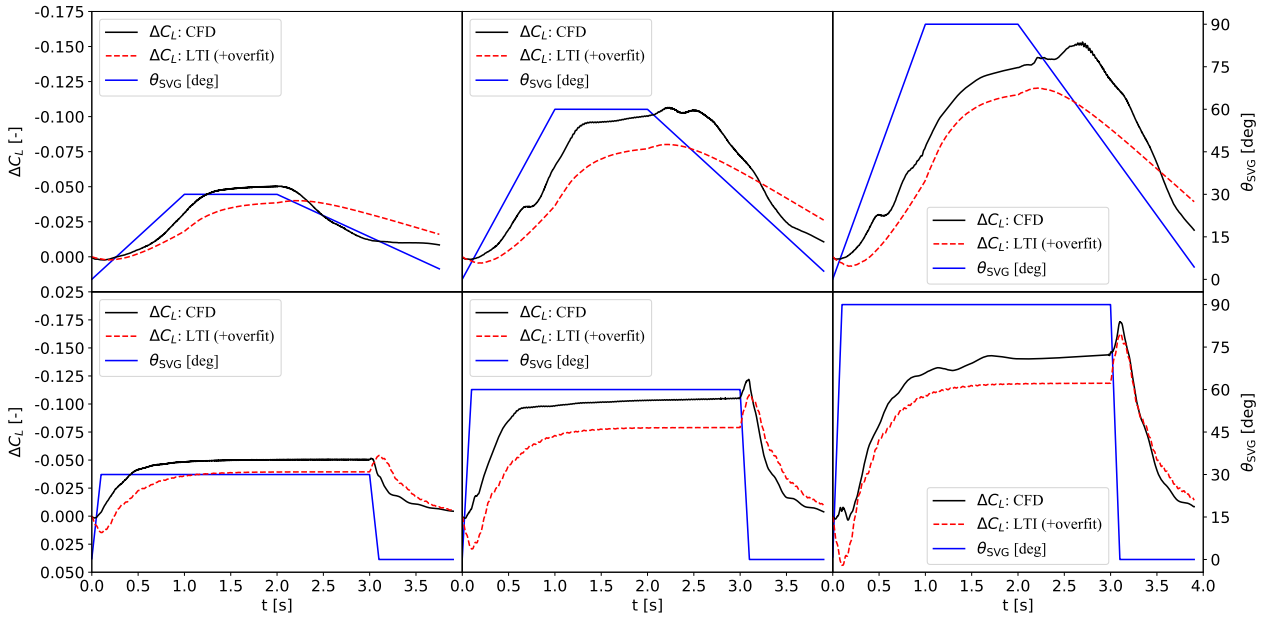

Fig. 9 Evolution of the aerodynamic loads due to slowly and fast actuated SVG. Comparison of SINDYc-AIC-identified minimum $\widehat{\text{AIC}}$ ROM model with CFD measurements. ROM predictions were computing using coupled structural-aerodynamic solver with zero initial conditions.

nonlinear behavior to be captured without resorting to black-box representations.

$$\begin{aligned} \dot{\boldsymbol{x}} &= \boldsymbol{A}(\boldsymbol{p}(t))\boldsymbol{x} + \boldsymbol{B}(\boldsymbol{p}(t))\boldsymbol{u} \\ \boldsymbol{y} &= \boldsymbol{C}(\boldsymbol{p}(t))\boldsymbol{x} + \boldsymbol{D}(\boldsymbol{p}(t))\boldsymbol{u} \end{aligned} \tag{17}$$

Finally, the design of experiments plays a critical role in the success of system identification, particularly given the short duration and high cost of CFD simulations, where a single configuration requires weeks of computation. While persistent excitation is the golden standard, it may not be optimal in this context. The excitation should span the anticipated operational envelope of the system to ensure relevance for deployment, while also exploring other regions of the state space in order to potentially uncover non-intuitive physical mechanisms, which might be exploited by the controller[‖]. To this end, step-like and slower-varying deployment and retraction of the SVG were considered for system identification purposes—mimicking the likely MPC control strategy of the SVG: quick deployment followed by more delicate retraction. Extrapolation beyond the training data set remains inherently risky for nonlinear systems and should be avoided unless supported by strong physical insight into the underlying dynamics.

The data used for identification of the LPV system corresponding to the ΔC_L and ΔC_M due to SVG motion was generated using CFD simulations which do allow heave and pitch motions. This was done to enable the identification of possible coupled effects between the wing motion and the SVG motion on the aerodynamic loads. In order to isolated the changes in aerodynamic loads due to SVG motion and its coupling with wing motion only, aerodynamic loads due to the pure movement of the wing were subtracted from the (total) aerodynamic loads measured in CFD simulations by assuming their evolution follows the SINDYc-AIC-identified minimum $\widehat{\text{AIC}}$ model and overfit model given in subsection III.A. The model which best balances explainability and sparsity is given in Equation 18. The control input and scheduling parameter is the Küssner-filtered SVG rotation angle, θ_{SVG}. More than two hidden states ($\boldsymbol{x} \in \mathbb{R}^{d_x>2}$) did not result in better fit.

$$\begin{aligned} \dot{\boldsymbol{x}} &= (\boldsymbol{A}_{\text{LTI}} + p(u)\boldsymbol{A}_{\text{LPV}})\,\boldsymbol{x} + (\boldsymbol{B}_{\text{LTI}} + p(u)\boldsymbol{B}_{\text{LPV}})\,u \quad ; \quad u = p(u) = \theta_{\text{SVG}} * h_{\text{Küssner}} \\ \boldsymbol{y} &= (\boldsymbol{C}_{\text{LTI}} + p(u)\boldsymbol{C}_{\text{LPV}})\,\boldsymbol{x} + (\boldsymbol{D}_{\text{LTI}} + p(u)\boldsymbol{D}_{\text{LPV}})\,u \quad ; \quad \boldsymbol{y} = [\Delta C_L, \Delta C_M]^\top \end{aligned} \tag{18}$$

[‖]Within the context of this study, this could be achieved by prescribing heave, pitch and SVG motion, instead of only prescribing SVG motion and observing the natural response of the structural dynamics due to SVG forcing. It would also allow to prescribe control signals which are highly orthogonal, resulting in better conditioning of the regression problem.

Results corresponding to the LPV system defined in Equation 18 are given in Figure 10a and Figure 10b for the LPV system based on the residual aerodynamic loads obtained by removing the wing-motion-induced loads predicted by the SINDYc-AIC-identified minimum $\widehat{\text{AIC}}$ model (Equation 14), for slowly and fast varying SVG angle θ_{SVG}, respectively. Analogously, Figure 11a and Figure 11b, show similar results for LPV system based on the residual loads obtained by removing the wing-motion-induced loads predicted by the overfit model (Equation 16). All of the figures, however, show the total changes in ΔC_L and ΔC_M by integrating the coupled structural and aerodynamic reduced-order dynamical models in time from zero initial condition.

These results show that the non-minimum-phase behavior at high angles of SVG deployment are easily captured by the proposed LPV system. While phase error has been mitigated completely in both LPV system (corresponding to SINDYc-AIC-identified minimum $\widehat{\text{AIC}}$ and overfit model of the wing-gust system), amplitude mismatch is present in the system corresponding to the SINDYc-AIC-identified minimum $\widehat{\text{AIC}}$ model of the wing-gust system. This is expected behavior as amplitude mismatch is present in the pure wing-gust system of this underlying wing-gust model too (see Figure 6a).

IV. Conclusion

This work has firstly utilized Akaike information criterion for model selection of wing-gust dynamic system based on CFD data. It has been shown that the dominant part of aerodynamic loads are due to the presence of the wind gust and the associated movement in heave degree of freedom. Secondly, wing-SVG dynamic system has been identified as linear parameter-varying. This is supported by the initial identification of the type of nonlinearity present in the system using initial regression to linear time-invariant system. The dominant nonlinearity is the absence of non-minimum phase behavior at low angles of SVG deployment, and strong presence of non-minimum phase behavior at high angles of SVG deployment. This system identification process has been accompanied with snapshots of the flow field data, making the system identification process more explainable than pure system-theoretic point of view.

V. Future Work

Future work includes identification of the wing-gust-SVG system using LPV system in combination with (STLSQ) algorithm in SINDYc fashion. Scheduling parameters, as well as the number of hidden states, contribute towards the degree of explanatory variables in the definition of AIC, while different candidates for the LPV scheduling parameter resemble the candidate library within SINDYc framework, which can be optimized using sparsity promoting regularization algorithm, such as STLSQ. Model predictive controller can then be deployed on the fully coupled system within ROM framework for online control purposes within validatory CFD simulations.

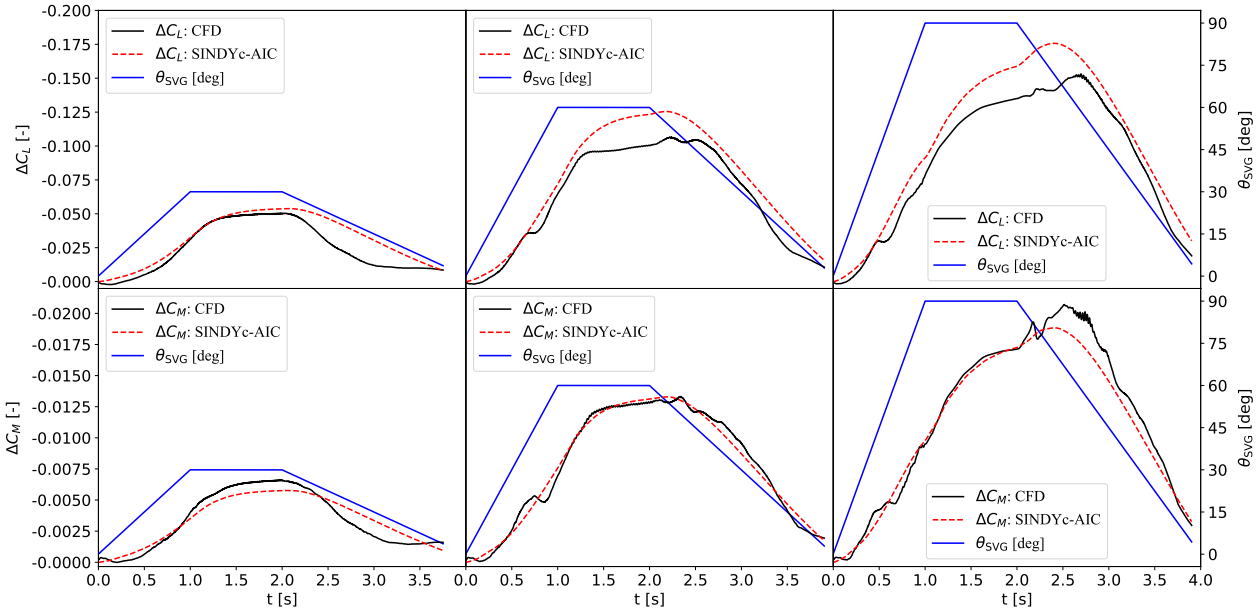

(a) Evolution of the aerodynamic loads due to slowly actuated SVG. Comparison of SINDYc-AIC-identified minimum $\widehat{\text{AIC}}$ ROM model in combination with LPV ROM model with CFD measurements. ROM predictions were computing using coupled structural-aerodynamic solver with zero initial conditions.

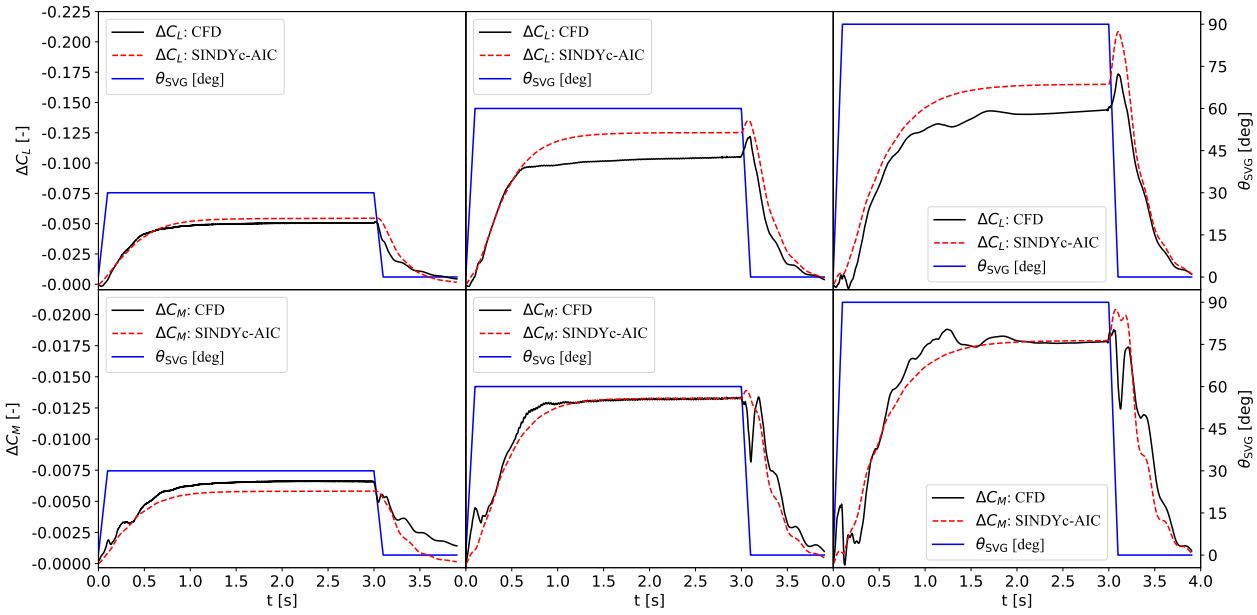

(b) Evolution of the aerodynamic loads due to fast actuated SVG. Comparison of SINDYc-AIC-identified minimum $\widehat{\text{AIC}}$ ROM model in combination with LPV ROM model with CFD measurements. ROM predictions were computing using coupled structural-aerodynamic solver with zero initial conditions.

Fig. 10 Evolution of the aerodynamic loads due to slowly (ramp function) and fast (step function) actuated SVG. Comparison of SINDYc-AIC-identified minimum $\widehat{\text{AIC}}$ ROM model in combination with LPV ROM model with CFD measurements. ROM predictions were computing using coupled structural-aerodynamic solver with zero initial conditions.

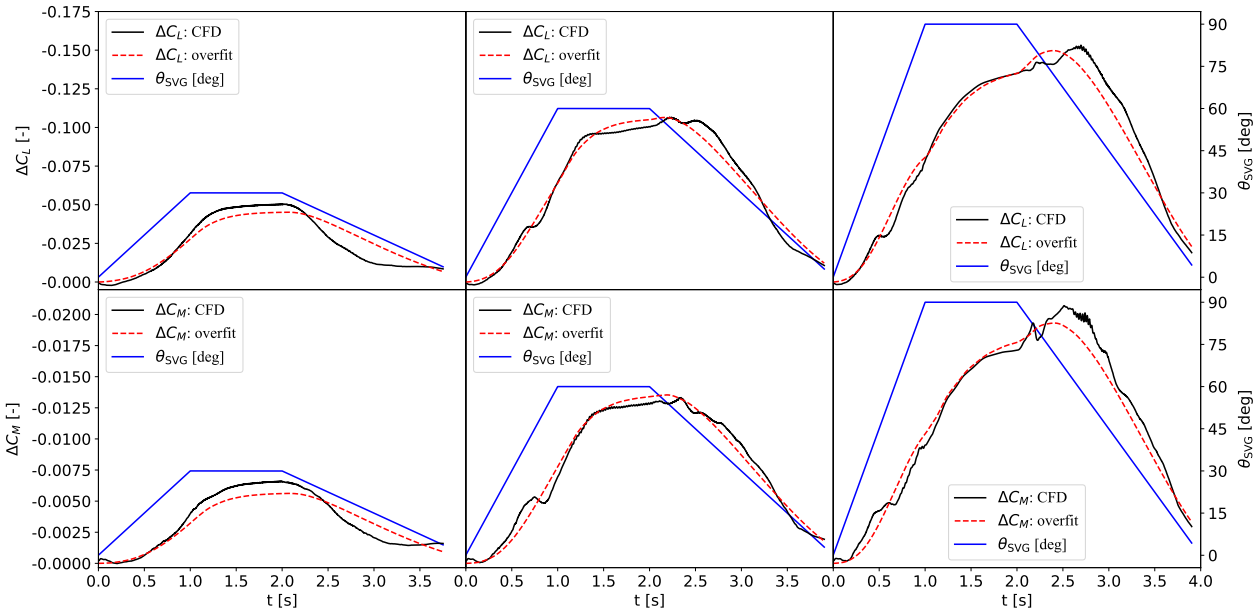

(a) Evolution of the aerodynamic loads due to slowly actuated SVG. Comparison of the overfit ROM model in combination with LPV ROM model with CFD measurements. ROM predictions were computing using coupled structural-aerodynamic solver with zero initial conditions.

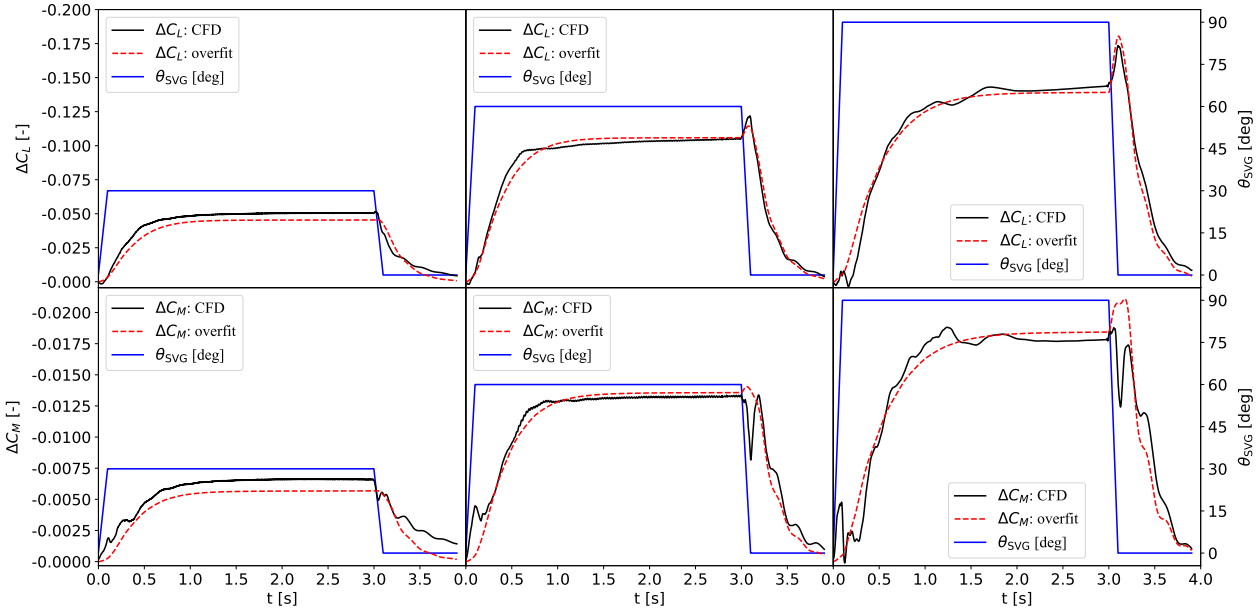

(b) Evolution of the aerodynamic loads due to fast actuated SVG. Comparison of the overfit ROM model in combination with LPV ROM model with CFD measurements. ROM predictions were computing using coupled structural-aerodynamic solver with zero initial conditions.

Fig. 11 Evolution of the aerodynamic loads due to slowly (ramp function) and fast (step function) actuated SVG. Comparison of the overfit ROM model in combination with LPV ROM model with CFD measurements. ROM predictions were computing using coupled structural-aerodynamic solver with zero initial conditions.

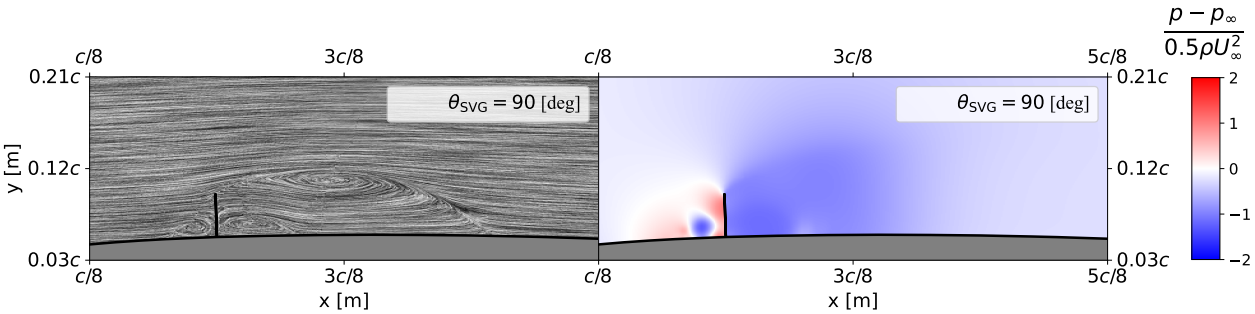

(a) Line integral convolution (LIC) of the velocity field (left) and pressure contour (right) within the vertical plane through the middle of the wing. Massive flow separation is clearly visible, including three vortices (one in front of the SVG and two behind the SVG). This is supported by the low pressure regions present in the pressure contour plot.

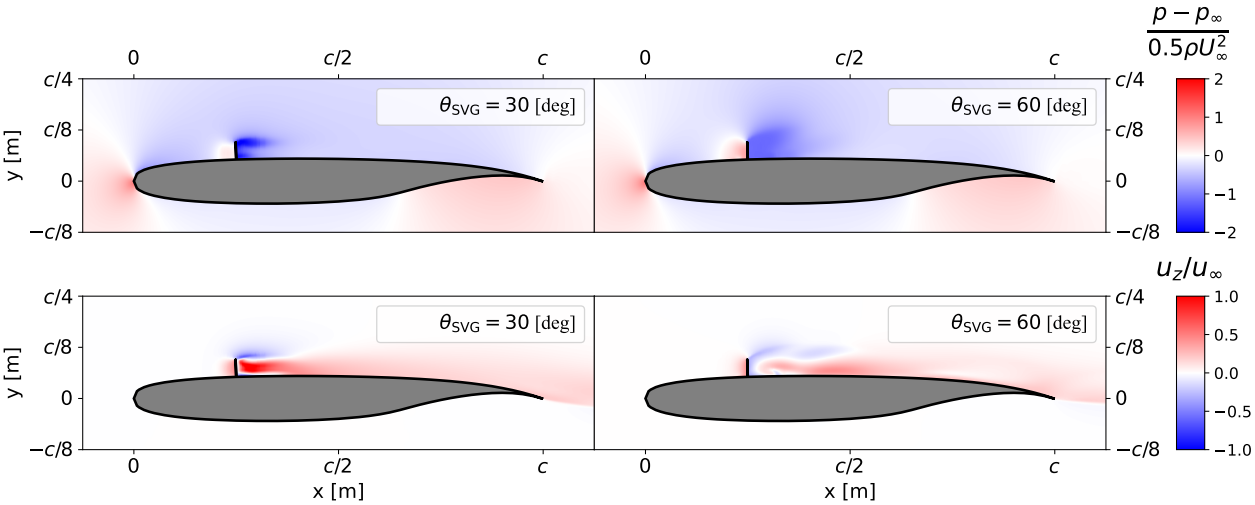

(b) Pressure contour plots and out-of-page velocity contour plots within the vertical plane through the middle of the wing for two angles of SVG deployment. Downstream convected vortices are clearly present behind the SVG. Moreover, the entire flow field is skewed in the direction of SVG rotation behind the SVG.

Fig. 12 Velocity (including line integral convolution (LIC)) and pressure contour plots of airflow actuated by SVG deflection.

References

[1] Eberle, A., Stefes, B., and Reckzeh, D., "Clean Aviation Ultra-Performance Wing (UP-Wing)," *AIAA SCITECH 2024 Forum*, American Institute of Aeronautics and Astronautics Inc. (AIAA), 2024. https://doi.org/10.2514/6.2024-2109, URL https://arc.aiaa.org/doi/abs/10.2514/6.2024-2109.

[2] Pohl, J. E., Radespiel, R., Herrmann, B., Brunton, S. L., and Semaan, R., "Gust mitigation through closed-loop control. I. Trailing-edge flap response," *Physical Review Fluids*, Vol. 7, No. 2, 2022, p. 024705. https://doi.org/10.1103/PhysRevFluids.7.024705, URL https://link.aps.org/doi/10.1103/PhysRevFluids.7.024705, publisher: American Physical Society.

[3] Herrmann, B., Brunton, S. L., Pohl, J. E., and Semaan, R., "Gust mitigation through closed-loop control. II. Feedforward and feedback control," *Physical Review Fluids*, Vol. 7, No. 2, 2022, p. 024706. https://doi.org/10.1103/PhysRevFluids.7.024706, URL https://link.aps.org/doi/10.1103/PhysRevFluids.7.024706, publisher: American Physical Society.

[4] Al-Battal, N. H., Cleaver, D. J., and Gursul, I., "Lift reduction by counter flowing wall jets," *Aerospace Science and Technology*, Vol. 78, 2018, pp. 682–695. https://doi.org/https://doi.org/10.1016/j.ast.2018.05.025, URL https://www.sciencedirect.com/science/article/pii/S1270963817323118.

[5] Williams, D. R., and King, R., "Alleviating Unsteady Aerodynamic Loads with Closed-Loop Flow Control," *AIAA Journal*, Vol. 56, No. 6, 2018, pp. 2194–2207. https://doi.org/10.2514/1.J056817, URL https://doi.org/10.2514/1.J056817.

[6] Marino, L., Kiat, I., Eberle, A., and Sodja, J., "Parametric study of a switchable vortex generator for load alleviation in transonic conditions," *AIAA SCITECH 2024 Forum*, American Institute of Aeronautics and Astronautics Inc. (AIAA), 2024. https://doi.org/10.2514/6.2024-2110, URL https://arc.aiaa.org/doi/abs/10.2514/6.2024-2110.

[7] Pant, S. S., "Aeroelastic Study of Leading Edge Minitabs for Gust Load Alleviation," Master's thesis, Delft University of Technology, 2024.

[8] Marino, L., Eberle, A., and Sodja, J., "Three-Dimensional Parametric Analysis of a Switchable Vortex Generator for Aerodynamic Load Alleviation at Transonic Speeds," *AIAA SCITECH 2025 Forum*, American Institute of Aeronautics and Astronautics Inc. (AIAA), 2025. https://doi.org/10.2514/6.2025-0035, URL https://arc.aiaa.org/doi/abs/10.2514/6.2025-0035.

[9] *Volume 3 Applications: Volume 3: Applications*, De Gruyter, 2020. https://doi.org/10.1515/9783110499001, URL https://www.degruyterbrill.com/document/doi/10.1515/9783110499001/html.

[10] Deng, N. Yan, Y. Ji, C. and Noack, B. R., "Feature-based manifold modeling for the quasiperiodic wake dynamics of a pair of side-by-side cylinders," *Physics of Fluids*, Vol. 36, No. 9, 2024, p. 093613. https://doi.org/10.1063/5.0224579, URL https://doi.org/10.1063/5.0224579.

[11] Brunton, S. L., Proctor, J. L., and Kutz, J. N., "Sparse Identification of Nonlinear Dynamics with Control (SINDYc)," *IFAC-PapersOnLine*, Vol. 49, No. 18, 2016, pp. 710–715. https://doi.org/https://doi.org/10.1016/j.ifacol.2016.10.249, URL https://www.sciencedirect.com/science/article/pii/S2405896316318298, 10th IFAC Symposium on Nonlinear Control Systems NOLCOS 2016.

[12] Tibshirani, R., "Regression Shrinkage and Selection Via the Lasso," *Journal of the Royal Statistical Society: Series B (Methodological)*, Vol. 58, No. 1, 1996, pp. 267–288. https://doi.org/https://doi.org/10.1111/j.2517-6161.1996.tb02080.x, URL https://rss.onlinelibrary.wiley.com/doi/abs/10.1111/j.2517-6161.1996.tb02080.x.

[13] Brunton, S. L., Proctor, J. L., and Kutz, J. N., "Discovering governing equations from data by sparse identification of nonlinear dynamical systems," *Proceedings of the National Academy of Sciences*, Vol. 113, No. 15, 2016, pp. 3932–3937. https://doi.org/10.1073/pnas.1517384113, URL https://www.pnas.org/doi/abs/10.1073/pnas.1517384113.

[14] Chakrabarti, A., and Ghosh, J. K., "AIC, BIC and Recent Advances in Model Selection," *Philosophy of Statistics*, Handbook of the Philosophy of Science, Vol. 7, edited by P. S. Bandyopadhyay and M. R. Forster, North-Holland, Amsterdam, 2011, pp. 583–605. https://doi.org/https://doi.org/10.1016/B978-0-444-51862-0.50018-6, URL https://www.sciencedirect.com/science/article/pii/B9780444518620500186.

[15] Mangan, N. M., Kutz, J. N., Brunton, S. L., and Proctor, J. L., "Model selection for dynamical systems via sparse regression and information criteria," *Proceedings of the Royal Society A: Mathematical, Physical and Engineering Sciences*, Vol. 473, No. 2204, 2017, p. 20170009. https://doi.org/10.1098/rspa.2017.0009, URL https://royalsocietypublishing.org/doi/abs/10.1098/rspa.2017.0009.

[16] Chakrabarti, A., and Ghosh, J. K., "AIC, BIC and Recent Advances in Model Selection," *Philosophy of Statistics*, Handbook of the Philosophy of Science, Vol. 7, edited by P. S. Bandyopadhyay and M. R. Forster, North-Holland, Amsterdam, 2011, pp. 583–605. https://doi.org/https://doi.org/10.1016/B978-0-444-51862-0.50018-6, URL https://www.sciencedirect.com/science/article/pii/B9780444518620500186.

[17] Kaheman, K., Kutz, J. N., and Brunton, S. L., "SINDy-PI: a robust algorithm for parallel implicit sparse identification of nonlinear dynamics," *Proceedings of the Royal Society A: Mathematical, Physical and Engineering Sciences*, Vol. 476, No. 2242, 2020, p. 20200279. https://doi.org/10.1098/rspa.2020.0279, URL https://royalsocietypublishing.org/doi/abs/10.1098/rspa.2020.0279.

[18] Peng, Z., Yao, X., Liu, H., and Huang, R., "Data-driven modeling of transonic nonlinear flutter via convolutional neural network autoencoder," *Nonlinear Dynamics*, Vol. 113, No. 13, 2025, pp. 15741–15760. https://doi.org/10.1007/s11071-025-10953-3, URL https://link.springer.com/article/10.1007/s11071-025-10953-3, company: Springer Distributor: Springer Institution: Springer Label: Springer Number: 13 Publisher: Springer Netherlands.

[19] Fonzi, N., Brunton, S. L., and Fasel, U., "Data-driven nonlinear aeroelastic models of morphing wings for control," *Proceedings of the Royal Society A: Mathematical, Physical and Engineering Sciences*, Vol. 476, No. 2239, 2020, p. 20200079. https://doi.org/10.1098/rspa.2020.0079, URL http://arxiv.org/abs/2002.03139, arXiv:2002.03139 [physics].

[20] Fonzi, N., Brunton, S. L., and Fasel, U., "Data-Driven Modeling for Transonic Aeroelastic Analysis," *Journal of Aircraft*, Vol. 61, No. 2, 2024, pp. 625–637. https://doi.org/10.2514/1.C037409, URL https://doi.org/10.2514/1.C037409, publisher: American Institute of Aeronautics and Astronautics _eprint: https://doi.org/10.2514/1.C037409.

[21] Sansica, A., Loiseau, J.-C., Kanamori, M., Hashimoto, A., and Robinet, J.-C., "System Identification of Two-Dimensional Transonic Buffet," *AIAA Journal*, Vol. 60, No. 5, 2022, pp. 3090–3106. https://doi.org/10.2514/1.j061001, URL https://hal.science/hal-03906486, publisher: American Institute of Aeronautics and Astronautics.

[22] Whitcomb, R. T., "Review of NASA supercritical airfoils," Tech. rep., National Aeronautics and Space Administration, Langley Research Center, 1974.

[23] Wöhler, S., Häßy, J., and Kriewall, V., "Establishing the DLR-F25 as a research baseline aircraft for the schort-medium range market in 2035," , Sep 2024. URL https://tore.tuhh.de/handle/11420/52124.

[24] Menter, F. R., "Two-equation eddy-viscosity turbulence models for engineering applications," *AIAA Journal*, Vol. 32, No. 8, 1994, pp. 1598–1605. https://doi.org/10.2514/3.12149, URL https://doi.org/10.2514/3.12149.

[25] Emeis, S., *Wind Energy Meteorology: Atmospheric Physics for Wind Power Generation*, Green Energy and Technology, Springer, Berlin, Heidelberg, 2013. https://doi.org/10.1007/978-3-642-30523-8, URL https://link.springer.com/10.1007/978-3-642-30523-8.

[26] Bos, R., "Extreme gusts and their role in wind turbine design," Ph.D. thesis, Delft University of Technology, 2017.

[27] EASA, "CS-25 Amendment 26: Certification specifications and acceptable means of compliance for large aeroplanes," Tech. rep., European Union Aviation Safety Agency, 2020.

[28] Heinrich, R., *Simulation of Interaction of Aircraft and Gust Using the TAU-Code*, Springer International Publishing, Cham, 2014, pp. 503–511. https://doi.org/10.1007/978-3-319-03158-3_51, URL https://doi.org/10.1007/978-3-319-03158-3_51.

[29] Wales, C., Jones, D., and Gaitonde, A., "Prescribed velocity method for simulation of aerofoil gust responses," *Journal of Aircraft*, Vol. 52, No. 1, 2015, pp. 64–76. https://doi.org/10.2514/1.C032597.

[30] Bisplinghoff, R., Ashley, H., and Halfman, R., *Aeroelasticity*, Dover Books on Aeronautical Engineering Series, Dover Publications, 1996.

[31] Akaike, H., "A new look at the statistical model identification," *IEEE Transactions on Automatic Control*, Vol. 19, No. 6, 1974, pp. 716–723. https://doi.org/10.1109/TAC.1974.1100705.

[32] Loiseau, J.-C., Noack, B. R., and Brunton, S. L., "Sparse reduced-order modelling: sensor-based dynamics to full-state estimation," *Journal of Fluid Mechanics*, Vol. 844, 2018, p. 459–490. https://doi.org/10.1017/jfm.2018.147.

[33] Billings, S., and Leontaritis, I., "Parameter Estimation Techniques for Nonlinear Systems," *IFAC Proceedings Volumes*, Vol. 15, No. 4, 1982, pp. 505–510. https://doi.org/https://doi.org/10.1016/S1474-6670(17)63039-8, URL https://www.sciencedirect.com/science/article/pii/S1474667017630398, 6th IFAC Symposium on Identification and System Parameter Estimation, Washington USA, 7-11 June.

[34] Cheng, C., Peng, Z., Zhang, W., and Meng, G., "Volterra-series-based nonlinear system modeling and its engineering applications: A state-of-the-art review," *Mechanical Systems and Signal Processing*, Vol. 87, 2017, pp. 340–364. https://doi.org/https://doi.org/10.1016/j.ymssp.2016.10.029, URL https://www.sciencedirect.com/science/article/pii/S0888327016304393.

[35] Juang, J.-N., Phan, M., Horta, L. G., and Longman, R. W., "Identification of observer/Kalman filter Markov parameters - Theory and experiments," *Journal of Guidance, Control, and Dynamics*, Vol. 16, No. 2, 1993, pp. 320–329. https://doi.org/10.2514/3.21006, URL https://doi.org/10.2514/3.21006.

[36] Ho, L., and Kalman, R. E., "Editorial: Effective construction of linear state-variable models from input/output functions," *at - Automatisierungstechnik*, Vol. 14, No. 1-12, 1966, pp. 545–548. https://doi.org/doi:10.1524/auto.1966.14.112.545, URL https://doi.org/10.1524/auto.1966.14.112.545.